https://doi.org/10.1016/j.electacta.2020.136535
This is the Pre-Published Version.

Microstructure-tuned cobalt oxide electrodes for high-performance Zn-Co batteries

Wenxu Shang[a], Wentao Yu[a], Xu Xiao[a], Yanyi Ma[a], Chun Cheng[b], Yawen Dai[b], Peng Tan[a*], Meng Ni[b,c*]

[a.] Department of Thermal Science and Energy Engineering, University of Science and Technology of China (USTC), Hefei 230026, Anhui, China.
[b.] Department of Building and Real Estate, The Hong Kong Polytechnic University, Hung Hom, Kowloon, Hong Kong, China.
[c.] Environmental Energy Research Group, Research Institute for Sustainable Urban Development (RISUD), The Hong Kong Polytechnic University, Hung Hom, Kowloon, Hong Kong, China.

* Corresponding authors:
Email: pengtan@ustc.edu.cn (Peng Tan)
Email: meng.ni@polyu.edu.hk (Meng Ni)

Abstract:

The insufficient utilization of active material results in the poor performance of Zn-Co batteries. In this work, by adjusting the key parameters in the synthesis process, the Co_3O_4 electrodes with different pore size distributions, morphologies, and loadings are fabricated. The effects of the tuned microstructures on three-electrode and battery systems are compared carefully. In this way, a heterogeneous porous nanowire structure with reasonable loading is constructed for the first time, which shows the optimal performance. Particularly, a Zn-Co battery with this electrode exhibits a high capacity of 230.0 mAh g^{-1} with a utilization ratio of 51.6% and a decent energy density of 308.8 Wh kg^{-1} based on the weight of Co_3O_4 and Zn plate. Besides, with an increase of the current densities from 0.5 to 10 A g^{-1}, the capacity drops from 230.0 to 144.0 mAh g^{-1} with the capacity retention of only 62.6%. Moreover, the battery can operate 3000 cycles (up to 547 h) with a retention ratio of 66.8%, illustrating excellent stability. This work gives an ultrahigh-capacity Co_3O_4

© 2020. This manuscript version is made available under the CC-BY-NC-ND 4.0 license http://creativecommons.org/licenses/by-nc-nd/4.0/

electrode benefiting from the novel-designed structure, which dramatically improves the utilization level of the active materials, leading to high and stable battery performance.

Keywords: microstructure optimization; cobalt oxide; zinc batteries, electrochemical performance

1. Introduction

Recently, searching for sustainable energy sources are in great need as a result of the fast consumption of fossil fuels. The successful application of fluctuating and intermittent renewable energy requires reliable and efficient energy storage. As one kind of energy storage strategies, batteries have obtained immense growth. For example, Li-ion batteries have been commercialized successfully because of their high energy density and stability [1–6]. However, a lot of issues like high cost (~90000 dollars per ton), potential danger, and health hazards have not been fully addressed [7–10]. In addition to Li-ion batteries, Zn-based batteries have attracted wide attention owing to the rich zinc resource, low price (~2500 dollars per ton), intrinsic safety, and decent theoretical capacity (825 mAh g_{Zn}^{-1}) [11–15]. To date, Zn batteries like Zn-Mn [16], Zn-NiO [17], and Zn-Ag [18] batteries have been explored extensively. The charging and discharging processes involve the oxidation and reduction of zinc metal and active materials [19]. However, limited by the insufficient theoretical capacity and low utilization of the positive electrode materials, the practical capacities are not attractive. For example, the operating capacity of a Zn-Ni battery is 165 mAh g^{-1}, only 46% of the theoretical value (360 mAh g^{-1}, calculated on

the mass of NiO), resulting in an insufficient energy density (228 Wh kg^{-1}) [20]. Thereby, new positive electrode materials with higher capacities are urgently needed [21].

Among zinc-based batteries, great progress of Zn-Co batteries has been achieved recently [22]. The Co-based material is considered as a great faradaic material due to its high theoretical capacity, high potential, great redox activity, and good reversibility [23,24]. However, restricted by the low electrical conductivity and small specific surface areas, the practical capacities are much lower than the theoretical ones [25,26]. As a kind of transition metal oxide, cobalt oxide (Co_3O_4) can be used as the positive electrode material, displaying a high theoretical capacity of 446 mAh g^{-1} and an operating voltage of up to 1.8 V in an alkaline Zn battery. For example, A Zn-Co_3O_4 battery assembled by Tan and coworkers exhibits a high capacity of 173.6 mAh g^{-1}, and a retention ratio of 66.6% at 5 A g^{-1} after 1000 cycles [27]. Wang et al. used the ultrathin porous nanosheet Co_3O_4@Ni foam, the battery showed a working voltage close to 1.8 V, an energy density of 241 W h kg^{-1}, and a capacity decay ratio of 20% after 2000 cycles [28]. Even with the promising achievements, considering the theoretical capacity of Co_3O_4, the utilization of the active materials is still insufficient (less than 50%), resulting in the waste of capacity. Besides using alkaline electrolytes, a Zn battery assembled with Co(III) rich-Co_3O_4 applying a mild electrolyte can work under the voltage up to 2 V and has a decent capacity of 205 mAh g^{-1} [29]. In contrast, the potential of the Zn electrode in alkaline electrolytes (−1.22 V vs SHE) is more negative than the value in mild electrolytes (−0.76 V vs SHE) [30,31], providing the

possibility for a higher battery voltage. Besides, the hydrogen evolution reaction (HER) and the formation of inactive zinc hydrate (e.g., $Zn_4SO_4(OH)_6{\cdot}H_2O$) is severe in the mild electrolyte, which causes the poor reversibility of Zn electrode [32,33]. Moreover, Co_3O_4 can only transfer two electrons in the mild electrolyte ($Co_3O_4 \rightarrow CoO$) [29], much lower than that in alkaline one (four electrons, $Co_3O_4 \rightarrow CoO_2$). Hence, the theoretical capacity of Co_3O_4 in alkaline electrolytes is almost twice of that in the mild ones. To this end, we choose the KOH solution as the electrolyte in this work.

As the electrochemical reactions occur at the two-phase interfaces of active material and liquid electrolyte, to improve the utilization ratio of the active material, optimizing the microstructure to facilitate the ion transport and enhance the electric conductivity can effectively improve both the capacity and the rate performance [34–40]. Yu et al. fabricated Co_3O_4 from nanowire, nanowire-cluster to bulk, and found that the sample with the morphology of thin nanowire-cluster delivered optimal specific area capacitance of 1.92 F cm^{-2} and capacity retention ratio of 72.91% even after 3000 charge-discharge cycles [41]. Huang et al. synthesized different morphology of Co_3O_4 samples from hexagonal nanosheet to nanoflake and ultimately fabricated a nanoflake/nanowire hybrid structure that showed the highest specific capacity [42]. Jiang et al. fabricated β-MnO_2@C nanocomposites through the plasma-assisted milling strategy, which exhibited good conductivity and promoted electrolyte infiltration due to the abundant pore distributions, leading to high cycle stability with a capacity of 130 mAh g^{-1} for 400 cycles at 0.3 A g^{-1} [43]. Zhang et al.

reported an ultrathin $Ni(OH)_2$ nanowire on ZnNiCo-oxide, which showed a high specific capacitance of 94.67 F cm^{-3} when served into a fiber-shaped asymmetric supercapacitor [44]. Our previous research indicated that among the nanosheet, nanowire, and nanoplate structures, the nanowire structure exhibited the highest discharge capacity [45]. However, the effects of Co_3O_4 microstructures on the electrochemical behaviors are still lacking in detail, limiting the breakthrough of Zn-Co batteries with striking performance.

Herein, the microstructure of the Co_3O_4 electrode was carefully optimized in this work. As the morphology can be tuned easily through hydrothermal reactions, we changed the key parameters in syntheses, such as the calcination temperature, hydrothermal time, and composition ratio in the precursor solution to produce the Co_3O_4 electrodes with different pore size distributions, mass loadings, and morphologies. After that, the sample with the best performance was further tested, such as the discharge capacity, rate capability, and cycle behavior. To compare the electrochemical performance of the samples carefully, the measurement was carried out in both the three-electrode and the battery system. Based on the results, a nanowire Co_3O_4 electrode with a heterogeneous porous structure is constructed successfully. More importantly, it delivers the highest operating capacity (230.0 mAh g^{-1}) among other reported Zn-Co_3O_4 battery, decent rate performance, and good cycling stability.

2. Experimental

2.1 Electrode fabrication

First, to remove the oil and oxide, a piece of nickel foam (3 cm × 5 cm) was ultrasonically washed by acetone solution and dilute HCl solution, then dried overnight under vacuum before use. Next, the nickel foam was put into an autoclave with a 40 mL reactant solution. The nanostructured Co_3O_4 on the nickel foam was formed after the hydrothermal reaction and the heat-treatment process. Various parameters in the synthesis process of Co_3O_4, including the heat treatment temperature and time, hydrothermal temperature and time, compositions in the precursor solution, are summarized in Table S1 (Supporting Information). To fabricate different microstructures, the key parameters in synthesis were investigated, including the heat treatment temperature, hydrothermal time, and compositions in the precursor solution. 40 mL of water dissolved with 0.5-1.5 mmol of $Co(NO_3)_2 \cdot 6H_2O$, 3-6 mmol of NH_4F, and 8 mmol of $CO(NH_2)_2$ was mixed into the 50 ml autoclave. Subsequently, it was maintained at 120 °C for 3-12 h and cooled down naturally to ambient temperature. The reactions during the hydrothermal reaction are proposed as following equations [23,46]:

$$Co^{2+} + xF^- \rightarrow [CoF_x]^{(x-2)-} \quad (1)$$

$$Co(NH_2)_2 + H_2O \rightarrow 2NH_3 + CO_2 \quad (2)$$

$$CO_2 + H_2O \rightarrow CO_3^{2-} + 2H^+ \quad (3)$$

$$NH_3 \cdot H_2O \rightarrow NH_4^+ + OH^- \quad (4)$$

$$2[CoF_x]^{(x-2)-} + CO_3^{2-} + 2OH^- + nH_2O \rightarrow Co_2(OH)_2CO_3 \cdot nH_2O + 2xF^- \quad (5)$$

After that, these pre-treated samples were cleaned with deionized water and dried fully overnight. Ultimately, the heat treatment was conducted under 300-400 ^oC for 3

h, with the heating rate of 1 °C min^{-1}:

$$3Co_2(OH)_2CO_3 \cdot nH_2O+O_2 \xrightarrow{\Delta} 2Co_3O_4 + 3(n+1)H_2O+3CO_2 \quad (6)$$

The mass loading of the Co_3O_4 was obtained by measuring the difference between the synthesized sample and the pristine nickel foam.

2.2 Material characterization

The material characterizations were conducted at the Experimental Center of Engineering and Material Sciences in USTC. In detail, the morphologies and nanostructures were characterized by a scanning electron microscope (SEM, XL-30 ESEM). The specific surface areas and the corresponding pore volumes were determined by the nitrogen adsorption-desorption isotherms of Co_3O_4-grown nickel foam, which were tested using a Tristar II 3020M surface area and porosity analyzer.

2.3 Electrochemical analyses

The electrochemical performance in the standard three-electrode system was measured by an electrochemical workstation (Solartron EnergyLab). The Co_3O_4 on Ni foam was applied as the working electrode, and a platinum plate and Hg/HgO were selected as the counter and reference electrodes, respectively, with a 1 M KOH solution. To obtain the cycle voltammetry (CV), the samples were tested in the voltage range between 0.1 and 0.7 V (vs. Hg/HgO) under different scan rates from 1 to 20 mV s^{-1}. The specific capacitance values (C) were calculated by:

$$C = \frac{1}{ms\Delta V}\int I(V)dV \quad (7)$$

where m, s, ΔV, and I(V) demonstrates the mass loading of Co_3O_4 (mg cm^{-2}), the scan rate (mV s^{-1}), the potential region, and the current density (mA cm^{-2}), respectively. To

characterize the double-layer capacitance (C_{dl}), the CV measurement was applied in the potential ranged between 0.15 and 0.21 V (vs. Hg/HgO). The C_{dl} values can be obtained from the slope plotted by capacitive currents using the scan rates of 2, 4, 6, and 8 mV s^{-1} [47]. All potentials were transformed to the reversible hydrogen electrode (RHE) scale in the result section.

2.4 Battery assembly and test

The samples were pouched into disc shapes with a diameter of 10 mm as positive electrodes. The electrode is assembled with a 0.5 mm-thick Zn plate and an aqueous solution involving 6 M KOH with 0.2 M $Zn(CH_3COO)_2$ to form a battery. To test the charge-discharge behavior, the batteries were measured at various current densities (A g^{-1}) and a fixed voltage region (i.e., 1.4-1.9 V). For a Zn-Co battery, the oxygen and hydrogen evolution reactions can occur dramatically under high voltage regions, which will cause high polarization due to the coverage of gas bubbles on the electrode. Besides, restricted by the consumption of active materials and insufficient ion transport, the voltage decreases rapidly below 1.5 V, and a deep discharge may deteriorate the reaction interfaces. Therefore, the voltage region from 1.4 to 1.9 V was selected to test the battery performance in this work. The charge/discharge capacity is calculated through the multiply of applied current density and corresponding charge/discharge time. The coulombic efficiency is calculated by the quotient of discharge and charge capacities. To evaluate the rate performance, the batteries were operated under various current densities (i.e., 0.5-10 A g^{-1}), while 2 A g^{-1} was set for the cycling behavior measurement.

3. Results and Discussion

3.1 Effects of calcination temperature

To research the effects of calcination temperature, the Co_3O_4 electrode was synthesized under the calcination temperatures of 300, 350, and 400 ^oC, and the loadings were measured to be 2.3, 2.14, and 2.02 mg cm^{-2}, respectively. The XRD results in Fig. S1 demonstrates that all samples are spinel Co_3O_4. Fig. 1 shows the SEM images of the samples using different calcination temperatures, from which all the samples show the nanowire morphology. However, as temperature increases, the nanowires become sparser. Moreover, the microstructure changes gradually. Under the temperature of 300 ^oC (Figs. 1a and 1b), the nanowire surface is almost smooth and hard to find pores. After increasing the temperature to 350 ^oC, interestingly, the sample shows uniform pores among the nanowire, as shown in the inset of Fig. 1d, which may provide abundant active sites for electrochemical reactions and benefit species transport [48,49]. When further increasing the temperature to 400 ^oC (Figs. 1e and 1f), the nanowires become thinner with irregular large pores, which may be ascribed from the extortionate calcination temperature [50]. To further investigate the microstructures of these samples, the isotherms and the corresponding pore size distributions were tested. As illustrated in Fig. 2a, the hysteresis loop for the one using 300 ^oC are type II and H3, while the samples using 350 and 400 ^oC are type II and H4. Besides, these samples show obvious pore size distribution differences (Fig. 2b). When the temperature increases from 300 to 350 and 400 ^oC, larger pores appear, and the size distribution shifts from 2-3 to 7-9 and 10-11 nm, respectively, consistent with

the SEM observations. Particularly, the sample under 350 ^{o}C shows three kinds of pores with the sizes of ~2, 3-4, and 5-10 nm, which is different from the reported Co_3O_4 electrode which usually owns a single pore structure. The heterogeneous structure leads to strong ability to be infiltrated by the electrolyte and facilitate the ions transfer. Moreover, this sample exhibits the nanowire with a diameter of ~70 nm, which is much lower than the reported value (e.g., ~1 μm in Ma' work [29]), leading to a high specific surface area. The specific surface areas are calculated to be 8.15, 9.81, and 4.47 m^2 g^{-1}, respectively, and the pore volumes are 0.0227, 0.0238, and 0.0188 cm^3 g^{-1}, respectively. The electrochemical surface area was also measured by the double-layer capacitance (C_{dl}), as shown in Fig. S2. the C_{dl} values for the samples under 300, 350, and 400 ^{o}C are 9.04, 17.09, and 6.65 mF cm^{-2}, respectively. Hence, the sample under 350 ^{o}C has the largest surface area and electrochemical surface area, indicating the advantage of the heterogeneous porous structure.

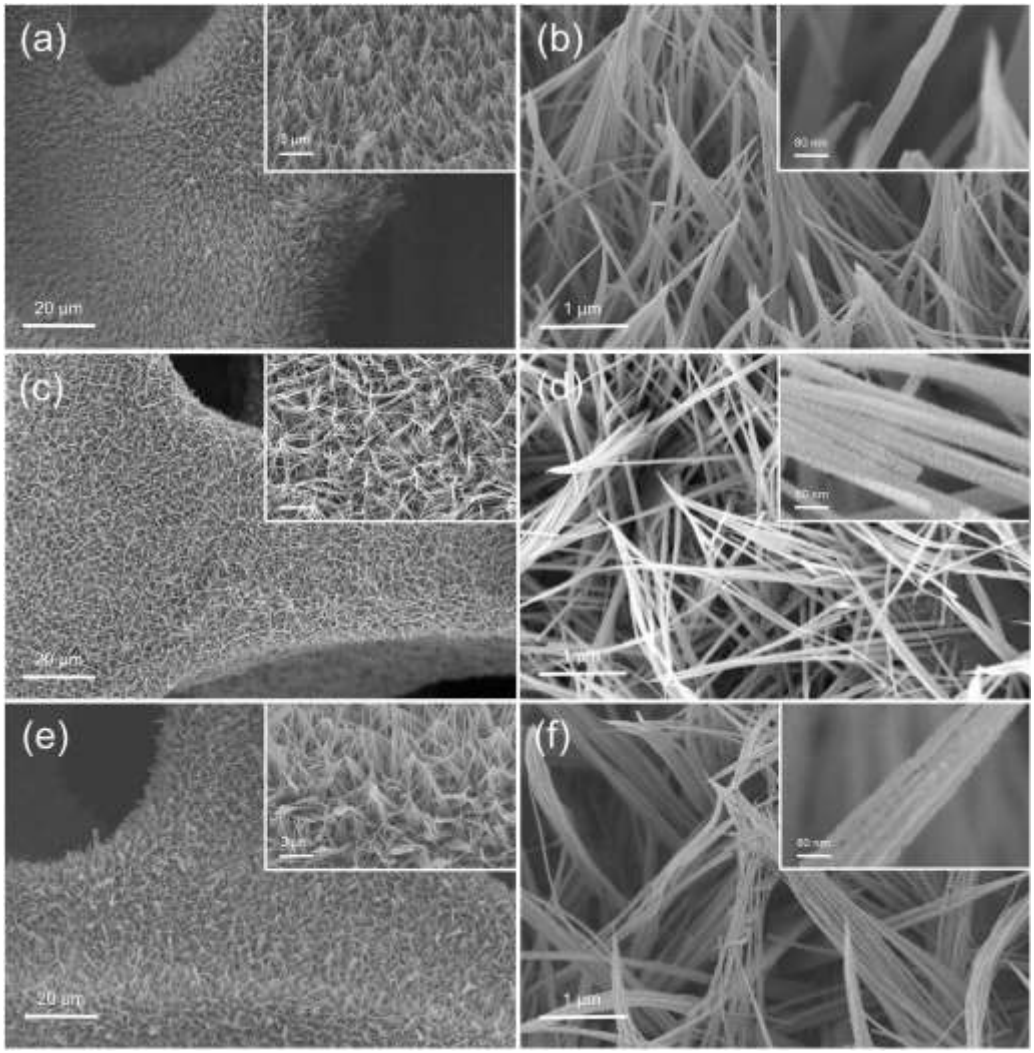

Fig. 1 SEM images of Co_3O_4 on Ni foam under different calcination temperatures. (a–b) 300 ºC, (c–d) 350 ºC, and (e–f) 400 ºC.

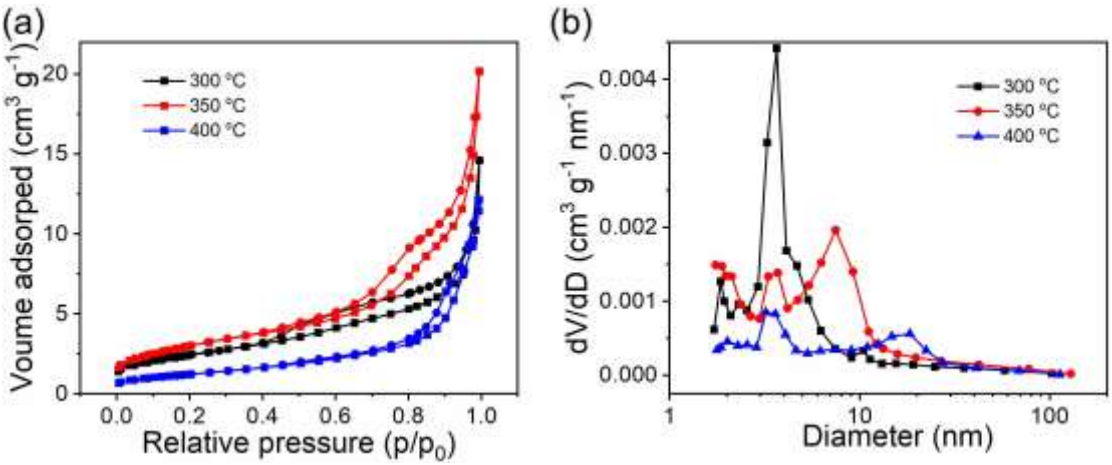

Fig. 2 Microstructure analyses of Co_3O_4 on Ni foam under different calcination

temperatures: (a) nitrogen adsorption-desorption isotherms and (b) the corresponding pore size distribution.

For the electrochemical performance, the samples under different temperatures show different CV curves at 10 mV s^{-1} in 1 M KOH solution (Fig. 3a). The one using 350 ^{o}C delivers the highest peak current density and the least potential difference between the oxidation and reduction peaks, manifesting the greatest reversibility. As illustrated in Fig. S3, the curve shapes maintain well at various scan rates from 1 to 20 mV s^{-1}, showing good rate performance. Fig. 3b shows the comparison of capacitance values from 1 to 20 mV s^{-1}, which are 714, 735, and 380 F g^{-1} under 300, 350, and 400 ^{o}C at 1 mV s^{-1}, respectively. Further, these samples were assembled into Zn batteries as the positive electrodes, and the charge-discharge voltage curves are displayed in Fig. 3c and S4. The batteries with the samples using 300, 350, and 400 ^{o}C show the operating capacities of 186.9, 218.7, and 145.6 mAh g^{-1} at 0.5 mA cm^{-2}, respectively. Besides, the sample using 350 ^{o}C exhibits the highest discharge and lowest charge voltage, indicating decent energy efficiency. To compare the rate performance of each sample, different current densities (0.5, 1, and 2 A g^{-1}) were carried out to test the capacities. As depicted in Fig. 3d, for the sample using 300 ^{o}C, at 0.5 and 2 A g^{-1}, the capacities are 186.7 and 173.3 mAh g^{-1}, respectively. When using 350 ^{o}C, the capacities are 218.7 and 204.9 mAh g^{-1}, respectively. While using 400 ^{o}C, the values are 145.8 and 132.2 mAh g^{-1}. Thus the corresponding capacity retention ratio can be calculated to 92.8%, 93.7%, and 90.6%, respectively. Hence, the calcination temperature changes the microstructure, thereby influences the

performance of the Co_3O_4. Specifically, the sample using the calcination temperature of 350 ^oC with the rational pore distribution microstructure exhibits the best electrochemical performance in both three-electrode and battery systems and thus is used as the calcination temperature in the following synthesis process.

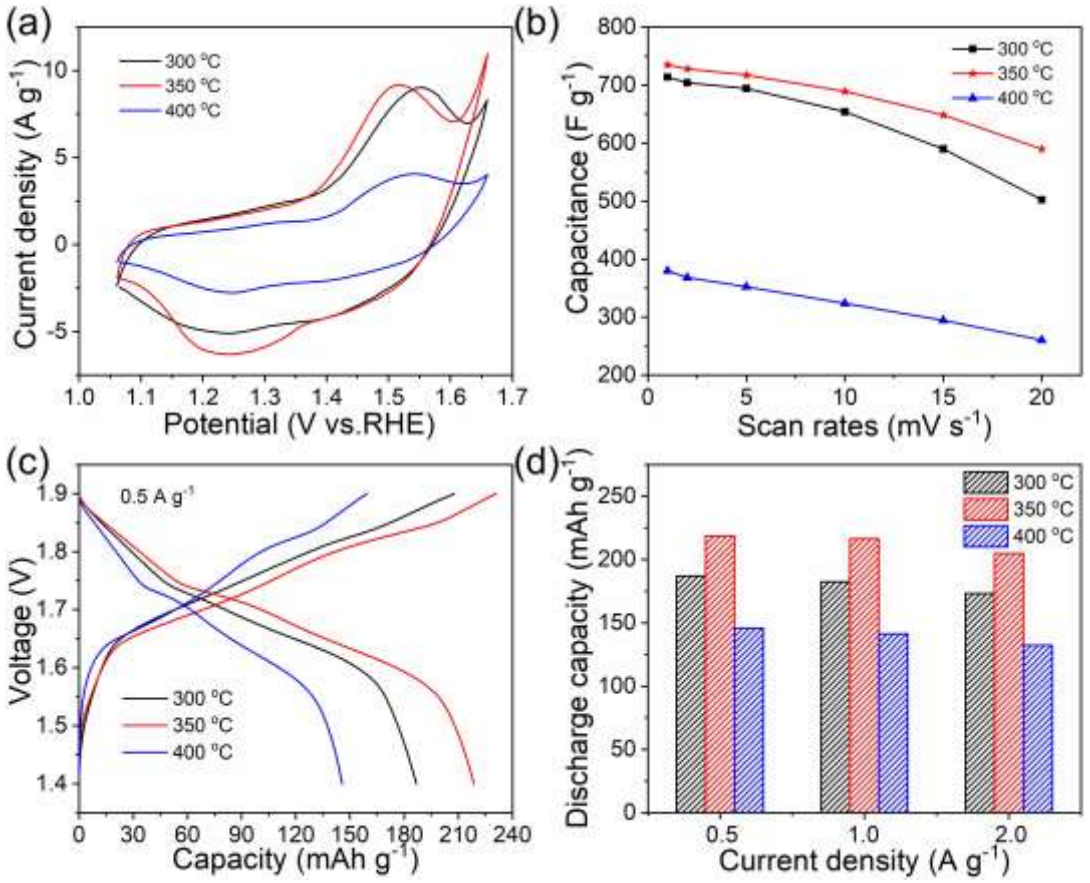

Fig. 3 Comparisons on the electrochemical performance of Co_3O_4 on Ni foam under different calcination temperatures: (a) the CV curves in 1 M KOH at 10 mV s^{-1}, (b) the specific capacitance at various scan rates from 1 to 20 mV s^{-1}, (c) the charge-discharge voltage curves at 0.5 A g^{-1}, and (d) comparison of operating capacity values at 0.5, 1, and 2 A g^{-1}.

3.2 Effects of hydrothermal time

Different hydrothermal time (i.e., 3, 6, 9, and 12 h) was then applied in the

synthesis process. To avoid repetition, only the SEM images of the samples under 3, 6, and 12 h are shown in Fig. 4. For the sample using the hydrothermal time of 3 h (Figs. 4a and 4b), the morphology of Co_3O_4 is nanowire-clusters, and the vertices of the nanowire-clusters are stacked together. When the time increases to 6 h (Figs. 4c and 4d), the nanowire-clusters bloom into the nanowire-flower and become denser. At the time of 9 h (Figs. 1c and 1d), the nanowire-flower becomes thinner and is coated uniformly on the nickel surface. When further increasing the time to 12 h (Figs. 4e and 4f), the nanowires become sparser.

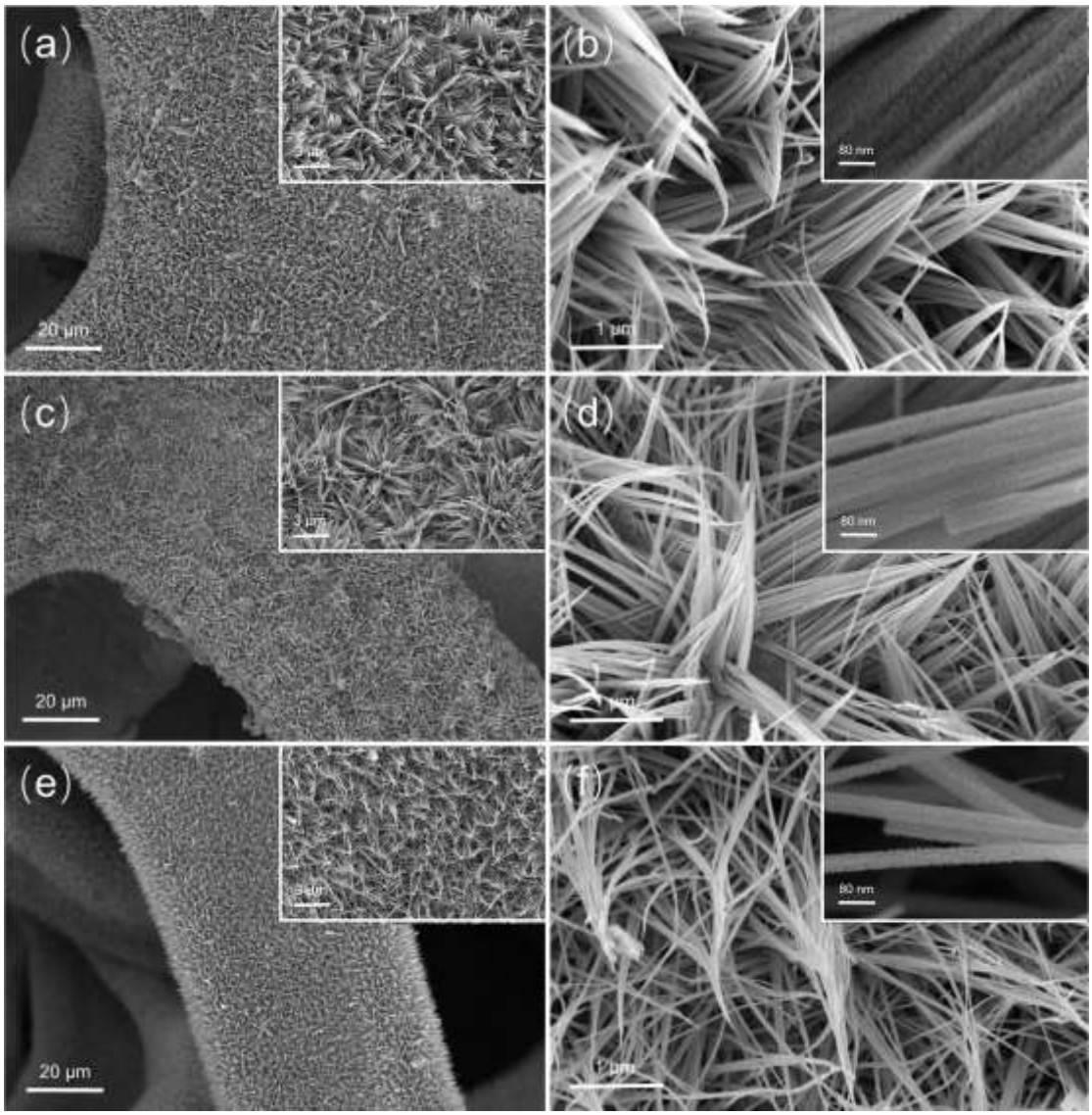

Fig. 4 SEM images of the Co_3O_4 on Ni foam using different hydrothermal time. (a–b) 3 h, (c–d) 6 h, and (e–f) 12 h.

The isotherms were tested to characterize the surface areas and pore volumes, as illustrated in Fig. S5. All of them can be classified as type II and H3, and the pore diameters are distributed around 1-10 nm. The specific surface areas are calculated to be 7.58, 12.09, and 8.99 $m^2 g^{-1}$, respectively, and the pore volumes are measured to be 0.0222, 0.0302, and 0.0275 $cm^3 g^{-1}$, respectively. Besides, when the time increases from 3, 6 to 12 h, the electrochemical surface areas are 14.22, 17.05, and 13.55 mF cm^{-2} (Fig. S6). Fig. 5a shows the CV comparisons at 10 mV s^{-1} in 1 M KOH, and the CV curves at various scan rates are depicted in Fig. S7. Although with similar CV shapes, the peak current densities change with an increase in the hydrothermal time. Fig. 5b displays the capacitance values of the samples at various scan rates, which are 670, 698, 735, 560 F g^{-1} at 1 mV s^{-1} for 3, 6, 9, 12 h, respectively.

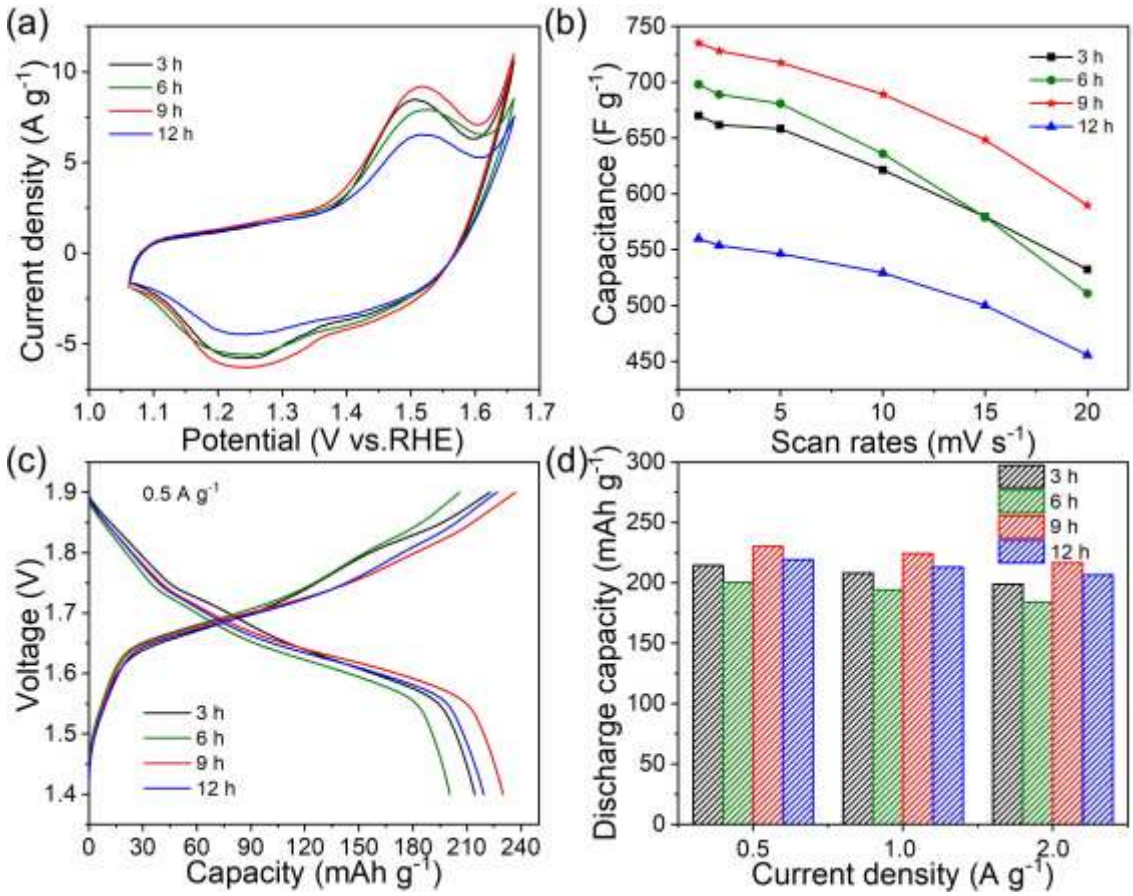

Fig. 5 Comparisons on the electrochemical performance of Co_3O_4 on Ni foam using different hydrothermal time. (a) the CV curves in 1 M KOH electrolyte at 10 mV s^{-1}, (b) the specific capacitance at different scan rates from 1 to 20 mV s^{-1}, (c) the charge-discharge voltage curves at 0.5 A g^{-1}, and (d) the discharge capacity values at 0.5, 1, and 2 A g^{-1}.

After assembling these samples into batteries, as shown in Fig. 5c, the discharge capacities are 214.4, 200.5, 230.0, and 219.5 mAh g^{-1} at 0.5 A g^{-1}, respectively. The charge and discharge capacities at 1 and 2 A g^{-1} are displayed in Fig. S8. Fig. 5d shows the comparison of the operating capacity values at the current densities of 0.5, 1, and 2 A g^{-1}. For the one using 3 h, the capacities are 214.4 and 198.8 mAh g^{-1} at 0.5 and 2 A g^{-1}, respectively, thus the retention ratio is 92.7%. In comparison, the

samples using 6 and 12 h have the capacity retention ratios of 91.7% and 94.1%. It is noting that the capacity of the one using 3 h is higher than the one using 6 h, which can be explained as the lower mass loading (2.03 mg cm^{-2}) that results in the lower electron transport resistance. For the CV test, the current is measured through varying the potential. Considering the actual mass loading (mg cm^{-2}), the current density (A g^{-1}) of the sample reveals the trend of fluctuation after normalization. While for the battery test, although the same current density (A g^{-1}) is set for the samples with different loadings, the actual current values (A) are different (the electrodes have the same surface area of 0.785 cm^2). For the sample at 6 h, the actual current (A) for discharge is relatively high due to the high loading. Moreover, the electric conductivity and the infiltration with electrolytes are inferior to other samples, which cause the lowest capacity value and poor rate stability. While for the sample at 12 h, the current is low due to the low loading, and the good electric conductivity and ability to infiltrate with electrolyte offset the lack of specific capacitance, leading to a higher discharge capacity than the one at 6 h. In conclusion, using different hydrothermal time, the mass loading of Co_3O_4 increases first, and achieves a maximum value (2.37 mg cm^{-2}) at 6 h, then decrease with the elongation reaction time of 12 h (2.20 mg cm^{-2}). Correspondingly, the nanowires are denser before 6 h, and thinner after the time. More importantly, as shown above, the Co_3O_4 synthesized using the hydrothermal time of 9 h has a reasonable loading and displays the best electrochemical performance, and thus is used as the best hydrothermal time in the following work.

3.3 Effects of chemical compositions of the precursor

In addition to the calcination temperature and hydrothermal reaction time, the molars of precursor chemicals (i.e., $Co(NO_3)_2 \cdot 6H_2O$, NH_4F, and urea) also have an important influence on the synthesis of Co_3O_4, as listed in Table S1. The reactions that occurred in the hydrothermal process can be described as Eqs. 1-6. First, as the source of Co element, different molars of $Co(NO_3)_2 \cdot 6H_2O$ (i.e., 0.5, 1, and 1.5 mmol) were applied, and the mass loadings of Co_3O_4 are 1.74, 2.26, and 3.37 mg cm^{-2}, respectively. To avoid repetition, Fig. 6 only illustrates the SEM images of the samples using 0.5 and 1.5 mmol $Co(NO_3)_2 \cdot 6H_2O$. When the amount is 0.5 mmol (Figs. 6a and 6b), the sample shows the morphology of condensed nanoplates, which is not beneficial for rapid ion transport and the reactions [51]. When the amount reaches 1 mmol (Figs. 1c and 1d), the morphology turns into the uniform nanowire. After increasing the amount to 1.5 mmol, the nanowires are coated densely on the Ni foam, as shown in Figs. 6c and 6d, which can be ascribed to the large mass loading. That is to say, different molars of $Co(NO_3)_2 \cdot 6H_2O$ change the morphology of Co_3O_4. Furthermore, the specific surface areas are 9.57 and 10.95 $m^2\ g^{-1}$, respectively, and the pore volumes are 0.0181 and 0.0311 $cm^3\ g^{-1}$, respectively (Fig. S9). It is worth noting that the one using 1.5 mmol has less nanopores but more mesopores, which may be the reason for the larger pore volume. The comparison of the electrochemical performance is also conducted. As displayed in Fig. S10, the C_{dl} values of the sample using 0.5 and 1.5 mmol $Co(NO_3)_2 \cdot 6H_2O$ are calculated as 11.12 and 16.66 mF cm^{-2}. Fig. 7a and S11 show their CV comparisons at 10 mV s^{-1} in 1 M KOH. The CV

shapes of the samples are similar, and the sample using 1 mmol $Co(NO_3)_2 \cdot 6H_2O$ shows the highest peak current density and decent reversibility. Fig. 7b shows the capacitance values of these samples based on different scan rates from 1 to 20 mV s^{-1}, which are 692.3, 735, and 603 F g^{-1} for 0.5, 1.0, and 1.5 mmol at 1 mV s^{-1}, respectively. When served as the battery electrodes, the charge-discharge voltage curves at 0.5 mA cm^{-2} are given in Fig. 5c, from which the operating capacities are 218.5, 230.0, and 154.7 mAh g^{-1} for the samples using the molar values of 0.5, 1.0, and 1.5 mmol, respectively. Even at other current densities (Fig. S12), the one using 1.0 mmol has the highest capacities, followed by the one using 0.5 mmol, and the capacities of the one using 1.5 mmol are the lowest, as given in Fig. 7d. Thus, the morphology and loading can be controllably changed through varying the amount of $Co(NO_3)_2 \cdot 6H_2O$ in the hydrothermal reaction solution. Particularly, the sample using 1.0 mmol with the evenly grown nanowire structure can deliver the best performance.

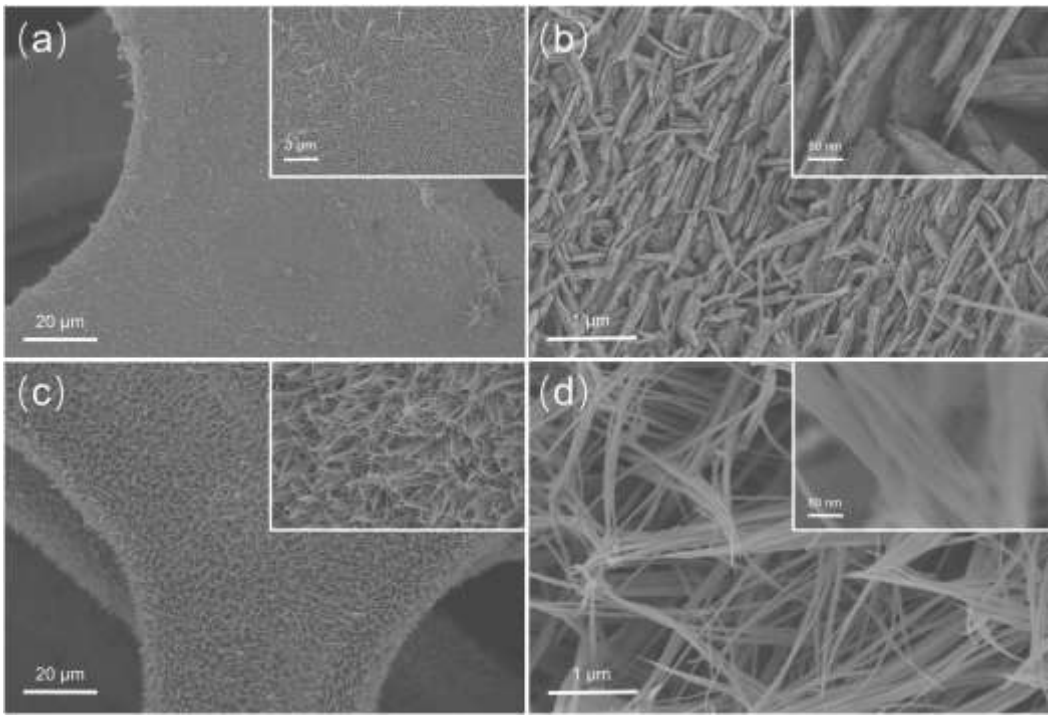

Fig. 6 SEM images of the Co_3O_4 on Ni foam using different molars of $Co(NO_3)_2 \cdot 6H_2O$. (a–b) 0.5 mmol and (c–d) 1.5 mmol.

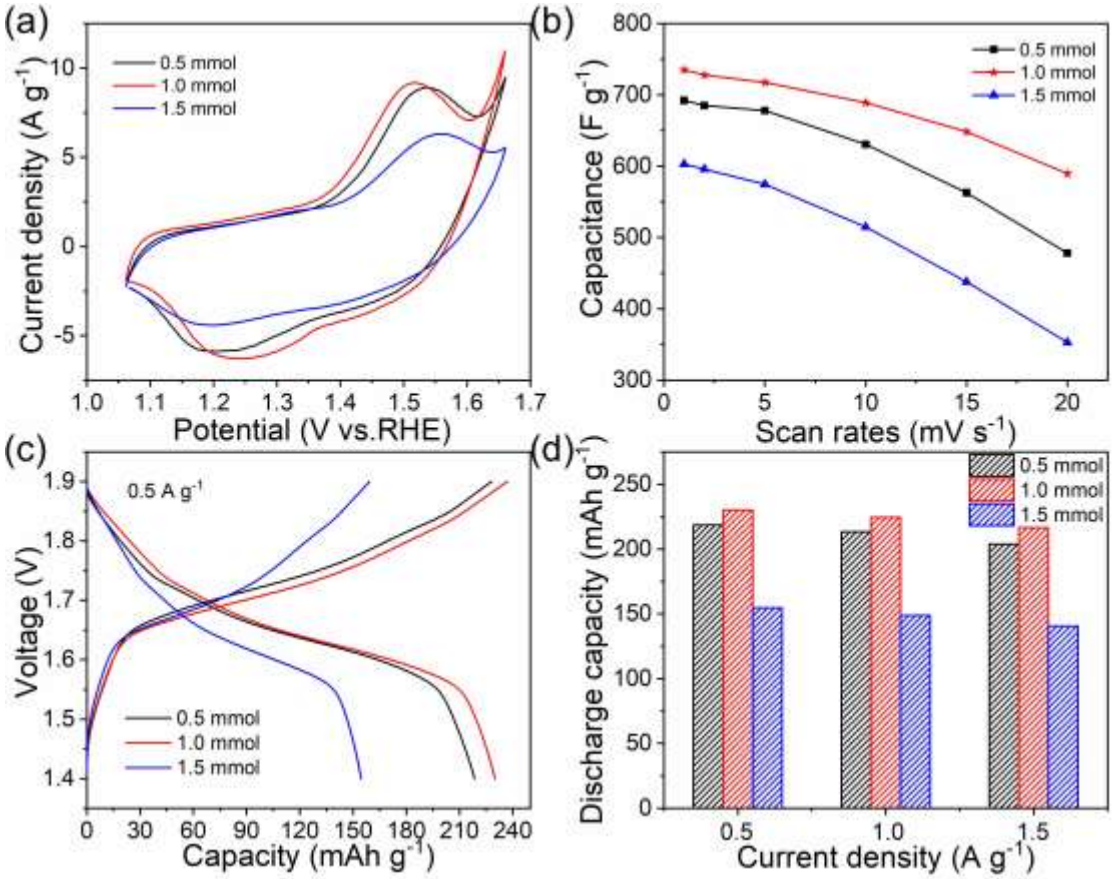

Fig. 7 Comparisons on the electrochemical performance of the Co_3O_4 on Ni foam using different molars of $Co(NO_3)_2 \cdot 6H_2O$: (a) the CV curves in 1 M KOH electrolyte at 10 mV s^{-1}, (b) the specific capacitance at various scan rates from 1 to 20 mV s^{-1}, (c) the charge-discharge voltage curves at 0.5 A g^{-1}, and (d) the operating capacity values at 0.5, 1, and 2 A g^{-1}.

Besides, as the additive in the precursor solution, NH_4F can combine with Co^{2+} to form $[CoF_x]^{(x-2)-}$. Previous reports have indicated that the presence of F^- have a great effect on reducing the nucleation rate and activating substrates, since F^- ions can combine with Co^{2+} at first and then release the Co^{2+} slowly [52]. Based on different

molars of NH_4F (i.e., 3, 4.5, 6 mmol), the samples show different mass loadings, which are 1.56, 2.26, 2.7 mg cm^{-2}, respectively. As displayed in Fig. S13 and Figs. 1c and 1d, the SEM images indicate that no morphology changes occur after changing the amount of NH_4F, and all nanowires are well-distributed on the surface of the Ni foam. In addition, the samples using the molars of 3 and 6 mmol displays the specific surface area of 8.13 and 8.70 m^2 g^{-1}, respectively, and the pore volume of 0.0226 and 0.0229 cm^3 g^{-1}, respectively. Fig. S14 gives the corresponding pore size distribution of the two samples. Although the distribution is similar in the range of 1-2 and 3-4 nm, the sample using 6 mmol NH_4F has larger pore volumes in the range of 5-10 nm than the one using 3 mmol, consistent with the SEM images. As for the double-layer capacitance (C_{dl}), the values for the samples using 3 and 6 mmol NH_4F are 11.79 and 7.37 mF cm^{-2}, respectively (Fig. S16). From Figs. S15a and S17, the sample using 4.5 mmol NH_4F delivers the highest peak current density and good reversibility. Moreover, as depicted in Fig. S15b, the capacitance value of the one using 4.5 mmol NH_4F is also the highest. Appling 0.5 A g^{-1}, the batteries with the samples using 3, 4.5, and 6 mmol show the discharge capacities of 225.5, 230.0, and 175.3 mAh g^{-1}, respectively (Fig. S15c). Notably, the batteries based on the samples using 3 and 4.5 mmol exhibit similar discharge capacities (Fig. S18), while the latter one delivers much larger specific surface area capacity (0.5152 mAh cm^{-2}) than the former (0.3583 mAh cm^{-2}), which can be ascribed to the high loading. Thus, the loading and the pore size distribution can be tuned using different molars of NH_4F, which then influence the electrochemical performance. Hence, 4.5 mmol NH_4F can be considered as the

optimal value for the synthesis.

3.4 Full-cell performance

To further test the full-cell performance, the electrode using the optimal synthesis conditions (i.e., 350 °C, 9 h, 1.0 mmol $Co(NO_3)_2 \cdot 6H_2O$, and 4.5 mmol NH_4F) was selected and assembled into a Zn battery for further tests. As provided in Table 1, the battery delivers a much higher value (230.0 mAh g^{-1}), accounting for 51.6% of the theoretical value, which is much higher than the reported one, such as 36.3% in Wang's work [28] and 38.9% in Tan's work [27]. It is noted that the theoretical capacity is calculated based on the transformation from Co_3O_4 to CoOOH and CoOOH to CoO_2 (i.e., $Co^{2+} \rightarrow Co^{3+} \rightarrow Co^{4+}$), the low utilization ratio indicates the conversion ability to high valence is limited. Hence, the reaction mechanism is valuable to be further studied. Figs. 8a and 8b reveal the charge-discharge voltage curves at different current densities in the voltage ranged between 1.4 and 1.9 V. When the current density increases from 0.5 to 10 A g^{-1}, the discharge capacity drops from 230.0 to 144.0 mAh g^{-1}, respectively, with coulombic efficiency of near 100%. The energy density drops from 380.6 to 225.0 mWh g^{-1}, and the corresponding energy efficiency changes from 93.5% to 87.7%. Hence, the battery delivers decent rate capability with the capacity retention of 62.6% even when the current density increases 20-fold, which is much better than the reported results in Table 1. For example, the Zn-Co battery with Co_3O_4 nanowires shows the retention rate of only 34% from 1 to 7.5 A g^{-1} [27], and the battery with Co_3O_4 nanosheets shows the retention of 48% from 1 to 10 A g^{-1} [28].

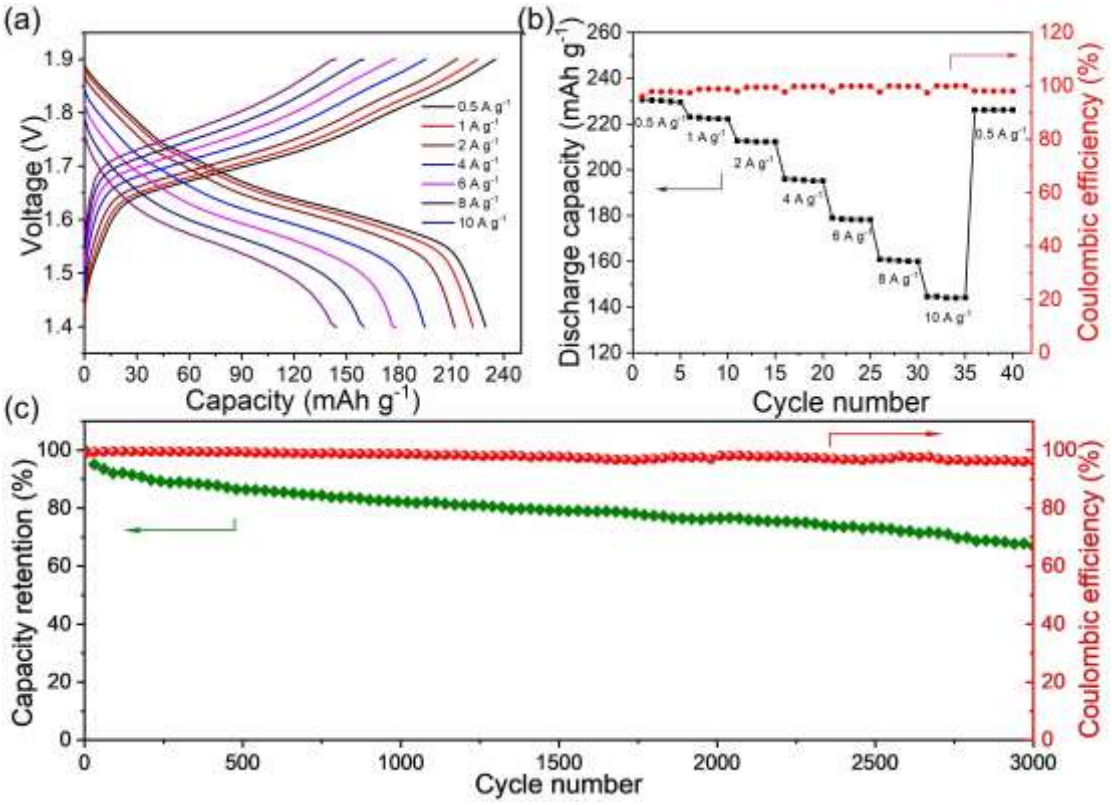

Fig. 8 Electrochemical performance of Zn battery with a heterogeneous porous nanowire Co_3O_4 nanowire on Ni foam electrode: (a) the charge-discharge voltage curves at various current densities from 0.5 to 10 A g^{-1}, (b) the operating capacity and coulombic efficiency at various current densities, and (c) the capacity retention and coulombic efficiency at various cycling numbers.

Furthermore, cycling behavior was tested at 2 A g^{-1} (Fig. 8c). As shown in Fig. S19, the shape of voltage curves retains well at different cycles, manifesting good reversibility. As the cycling life increases, the operating capacity drops to 178.9, 170.8, 164.4, and 156.4 mAh g^{-1} at the 500th to 1000th, 1500th, and 2000th cycle, respectively, thus the retention ratios are 85.2%, 81.3%, 78.3%, and 74.5%, respectively. Even after 3000 cycles with the operation time of up to 547 h, the battery can still operate and delivers the capacity retention of 66.8%, without any optimization of the zinc

electrode which has been regarded as the main cause for the performance decay [53–55]. Moreover, the coulombic efficiency was well maintained and almost close to 100%. After the cycling test, we conducted the SEM and XRD characterization of this electrode. As shown in Fig. S20, the nanowire structure maintained well even at the 3000^{th} cycle, and the peaks in the XRD pattern of the electrode barely changed, indicating its decent stability. In comparison, as shown in Table 1, the battery with Co_3O_4 nanowires can only perform 1000 cycles with a retention ratio of 66.6% at 5 A g^{-1} [27]. Although the battery using nanosheets and optimized zinc electrode shows a retention ratio of 80% after 2000 cycles at 1 A g^{-1}, the one without any optimizations of the positive electrode has the retention of 80% after only 900 cycles [28]. For the battery assembled with the Co_3O_4 nanowires@Ni wire and the fiber-shaped zinc electrode, it can only operate for 33 h with the capacity decay of 20% [22]. Hence, benefiting from the fast species transport, sufficient saturation between the electrolyte and the active material, and good electric conductivity, the electrode with the nanowire morphology and heterogeneous pore structure shows the largest capacity, remarkable cycling behavior, and great rate performance when compared to the reported alkaline Zn-Co batteries [22,27,28,56–61], demonstrating the promising potential for applications.

Table 1 Performance of the alkaline Zn batteries with various materials

Positive electrode materials	Loading	Electrochemical performance			Ref.
		Capacity	Cycling stability	Rate rentention	

Co_3O_4 nanowires@Ni wire	80±10 μg cm^{-1}	21.3 mAh cm^{-3}	80% after 3000 cycles (33 h)	77.9% from 0.25 to 2.5 A cm^{-3}	[22]
Co_3O_4 nanowire@Ni foam	3.9 mg cm^{-2}	173.6 mAh g^{-1}@1 A g^{-1}	66.6% after 1000 cycles at 5 A g^{-1}	34% from 1 to 7.5 A g^{-1}	[27]
Co_3O_4 nanosheets@Ni foam	2 mg cm^{-2}	162 mAh g^{-1}@1 A g^{-1}	80% after 900 cycles at 1 A g^{-1} (zinc plate); 80 % after 2000 cycles at 1 A g^{-1} (Zn@CF core–shell structure)	48% from 1 to 10 A g^{-1}	[28]
NiO-CNT	3 mg cm^{-2}	155 mAh g^{-1}	65% after 500 cycles at 1 A g^{-1}	52.9% from 1 to 3 A g^{-1}	[56]
Carbon cloth-carbon fiber@NiO	10.8 mg cm^{-2}	203 mAh g^{-1}	72.9% after 2400 cycles at 5 mA cm^{-2}	59.2% from 0.5 to 10 mA cm^{-2}	[57]
Ni-MOF-74/CNT fibers	0.4 mg cm^{-1}	108.5 mAh cm^{-3}	87.66% after 1000 cycles at 2 A cm^{-3}	60.4% from 0.5 to 5 A g^{-1}	[58]
Ni_3S_2 ultrathin nanosheets		150 mAh g^{-1}	83.3% after 100 cycles	45.9% from 0.2 to 5 A g^{-1}	[59]
Ni_2P@Carbon	1 mg cm^{-2}	176 mAh g^{-1}	93.8% after 1500 cycles	46.6% from 1 to 5 A g^{-1}	[60]
NiAlCo LDH nanoplates/CNTs	1 mg cm^{-2}	184 mAh g^{-1}	85% after 600 cycles	75% from 3.5 to 35 A g^{-1}	[61]
Heterogeneous porous nanowire Co_3O_4@Ni foam	2.24 mg cm^{-2}	230.0 mAh g^{-1}@0.5 A g^{-1}	66.8% after 3000 cycles at 2 A g^{-1} (up to 547 h)	62.6% from 0.5 to 10 A g^{-1}	Our work

4 Conclusions

In conclusion, through tuning the key parameters in synthesis, including the heat treatment temperature, hydrothermal time, and compositions in the precursor solution, Co_3O_4 on the Ni foam shows different pore size distributions, morphologies, and mass loadings. In detail, the pore size among the nanowire becomes larger with an increase of the calcination temperature. The loading can be controlled when using different hydrothermal time, and the morphology (i.e., condensed nanoplate and nanowire) can be tuned by changing the amount of $Co(NO_3)_2 \cdot 6H_2O$. From the electrochemical tests, the Co_3O_4 electrode with a heterogeneous porous nanowire structure and a reasonable loading exhibits the largest electrochemical surface area of 17.09 mF cm^{-2} and a specific capacitance value of 735 F g^{-1}. When assembled into a Zn battery, it delivers an optimal capacity of 230.0 mAh g^{-1} at 0.5 A g^{-1} and energy density of 308.8 Wh kg^{-1} calculated on the weight of Co_3O_4 and the Zn plate, achieving a high utilization ratio based on the theoretical value (up to 50%). Additionally, the capacity is 144.0 mAh g^{-1} at 10 A g^{-1}, thus the retention rate is 62.6%, manifesting great rate capability. More importantly, the battery exhibits an ultra-long cycling life of 3000 cycles (up to 547 h) with a retention ratio of 66.8%. Hence, this work tunes the microstructure of Co_3O_4 effectively and obtains a novel-designed heterogeneous porous electrode with a higher utilization ratio compared to other reported ones, achieving an ultrahigh-performance Zn-Co battery. To further optimize the microstructure and improve the performance, some other ways such as surface treatment can be also applied [62,63], which will be our future work.

Acknowledgments

P. Tan thanks the funding supports from CAS Pioneer Hundred Talents Program (KJ2090130001), USTC Research Funds of the Double First-Class Initiative (YD2090002006), Joint Laboratory for USTC and Yanchang Petroleum (ES2090130110), and USTC Tang Scholar. M. Ni thanks the funding support from The Hong Kong Polytechnic University (G-YW2D) and a grant (Project Number: PolyU 152214/17E) from Research Grant Council, University Grants Committee, Hong Kong SAR.

References

[1] A. Yoshino, The birth of the lithium-ion battery, Angew. Chemie. Int. Ed. 51 (2012) 5798–5800.

[2] L. Lu, X. Han, J. Li, J. Hua, M. Ouyang, A review on the key issues for lithium-ion battery management in electric vehicles, J. Power Sources. 226 (2013) 272–288.

[3] J. Jaguemont, L. Boulon, Y. Dubé, A comprehensive review of lithium-ion batteries used in hybrid and electric vehicles at cold temperatures, Appl. Energy. 164 (2016) 99–114.

[4] W. Li, Y. Yang, G. Zhang, Y.W. Zhang, Ultrafast and directional diffusion of lithium in phosphorene for high-performance lithium-ion battery, Nano Lett. 15 (2015) 1691–1697.

[5] D. Ma, Z. Cao, A. Hu, Si-based anode materials for li-ion batteries: A mini review, Nano-Micro Lett. 6 (2014) 347–358.

[6] H. Khalifa, S.A. El-Safty, A. Reda, M.A. Shenashen, M.M. Selim, A.

Elmarakbi, H.A. Metawa, Theoretical and Experimental Sets of Choice Anode/Cathode Architectonics for High-Performance Full-Scale LIB Built-up Models, Nano-Micro Lett. 11 (2019) 1–23.

[7] S. Abada, G. Marlair, A. Lecocq, M. Petit, V. Sauvant-Moynot, F. Huet, Safety focused modeling of lithium-ion batteries: A review, J. Power Sources. 306 (2016) 178–192.

[8] D. Ouyang, M. Chen, Q. Huang, J. Weng, Z. Wang, J. Wang, A Review on the thermal hazards of the lithium-ion battery and the corresponding countermeasures, Appl. Sci. 9 (2019) 2483.

[9] X. Han, L. Lu, Y. Zheng, X. Feng, Z. Li, J. Li, M. Ouyang, A review on the key issues of the lithium ion battery degradation among the whole life cycle, ETransportation. 1 (2019) 100005.

[10] Q. Wang, L. Jiang, Y. Yu, J. Sun, Progress of enhancing the safety of lithium ion battery from the electrolyte aspect, Nano Energy. 55 (2019) 93–114.

[11] W. Xu, Y. Wang, Recent Progress on Zinc-Ion Rechargeable Batteries, Nano-Micro Lett. 11 (2019) 1–30.

[12] P. Tan, B. Chen, H. Xu, W. Cai, W. He, H. Zhang, M. Liu, Z. Shao, M. Ni, Integration of Zn-Ag and Zn-Air Batteries: A Hybrid Battery with the Advantages of Both, ACS Appl. Mater. Interfaces. 10 (2018) 36873–36881.

[13] Y. Li, J. Fu, C. Zhong, T. Wu, Z. Chen, W. Hu, K. Amine, J. Lu, Recent Advances in Flexible Zinc-Based Rechargeable Batteries, Adv. Energy Mater. 9 (2019) 1802605.

[14] P. Tan, B. Chen, H. Xu, W. Cai, M. Liu, Z. Shao, M. Ni, Nanoporous $NiO/Ni(OH)_2$ Plates Incorporated with Carbon Nanotubes as Active Materials of Rechargeable Hybrid Zinc Batteries for Improved Energy Efficiency and High-Rate Capability, J. Electrochem. Soc. 165 (2018) A2119–A2126.

[15] H. Li, L. Ma, C. Han, Z. Wang, Z. Liu, Z. Tang, C. Zhi, Advanced rechargeable zinc-based batteries: Recent progress and future perspectives, Nano Energy. 62 (2019) 550–587.

[16] Y. Huang, J. Mou, W. Liu, X. Wang, L. Dong, F. Kang, C. Xu, Novel Insights into Energy Storage Mechanism of Aqueous Rechargeable Zn/MnO_2 Batteries with Participation of Mn^{2+}, Nano-Micro Lett. 11 (2019) 1–13.

[17] D.U. Lee, J. Fu, M.G. Park, H. Liu, A. Ghorbani Kashkooli, Z. Chen, Self-Assembled $NiO/Ni(OH)_2$ Nanoflakes as Active Material for High-Power and High-Energy Hybrid Rechargeable Battery, Nano Lett. 16 (2016) 1794–1802.

[18] S. Berchmans, A.J. Bandodkar, W. Jia, J. Ramírez, Y.S. Meng, J. Wang, An epidermal alkaline rechargeable Ag-Zn printable tattoo battery for wearable electronics, J. Mater. Chem. A. 2 (2014) 15788–15795.

[19] A. Sobianowska-Turek, W. Szczepaniak, P. Maciejewski, M. Gawlik-Kobylińska, Recovery of zinc and manganese, and other metals (Fe, Cu, Ni, Co, Cd, Cr, Na, K) from $Zn\text{-}MnO_2$ and Zn-C waste batteries: Hydroxyl and carbonate co-precipitation from solution after reducing acidic leaching with use of oxalic acid, J. Power Sources. 325 (2016) 220–228.

[20] W. Shang, W. Yu, P. Tan, B. Chen, Z. Wu, H. Xu, M. Ni, Achieving high energy density and efficiency through integration: Progress in hybrid zinc batteries, J. Mater. Chem. A. 7 (2019) 15564–15574.

[21] Y. Xu, Q. Li, H. Xue, H. Pang, Metal-organic frameworks for direct electrochemical applications, Coord. Chem. Rev. 376 (2018) 292–318.

[22] Q. Guan, Y. Li, X. Bi, J. Yang, J. Zhou, X. Li, J. Cheng, Z. Wang, B. Wang, J. Lu, Dendrite-Free Flexible Fiber-Shaped Zn Battery with Long Cycle Life in Water and Air, Adv. Energy Mater. (2019) 1901434.

[23] X. Zhang, J. Xiao, X. Zhang, Y. Meng, D. Xiao, Three-Dimensional Co_3O_4 Nanowires@Amorphous $Ni(OH)_2$ Ultrathin Nanosheets Hierarchical Structure for Electrochemical Energy Storage, Electrochim. Acta. 191 (2016) 758–766.

[24] C. Yuan, L. Yang, L. Hou, J. Li, Y. Sun, X. Zhang, L. Shen, X. Lu, S. Xiong, X.W. Lou, Flexible hybrid paper made of monolayer Co_3O_4 microsphere arrays on rGO/CNTs and their application in electrochemical capacitors, Adv. Funct. Mater. 22 (2012) 2560–2566.

[25] D. He, X. Song, W. Li, C. Tang, J. Liu, Z. Ke, C. Jiang, X. Xiao, Active electron density modulation of Co_3O_4 based catalysts endows highly oxygen evolution capability, Angew. Chemie Int. Ed. 59 (2020) 2–9.

[26] S. Sun, Y. Sun, Y. Zhou, S. Xi, X. Ren, B. Huang, H. Liao, L.P. Wang, Y. Du, Z.J. Xu, Shifting Oxygen Charge Towards Octahedral Metal: A Way to Promote Water Oxidation on Cobalt Spinel Oxides, Angew. Chemie Int. Ed. 58 (2019) 6042–6047.

[27] P. Tan, B. Chen, H. Xu, W. Cai, W. He, M. Ni, In-situ growth of Co_3O_4 nanowire-assembled clusters on nickel foam for aqueous rechargeable Zn-Co3O4 and Zn-air batteries, Appl. Catal. B Environ. 241 (2019) 104–112.

[28] X. Wang, F. Wang, L. Wang, M. Li, Y. Wang, B. Chen, Y. Zhu, L. Fu, L. Zha, L. Zhang, Y. Wu, W. Huang, An Aqueous Rechargeable Zn//Co_3O_4 Battery with High Energy Density and Good Cycling Behavior, Adv. Mater. 28 (2016) 4904–4911.

[29] L. Ma, S. Chen, H. Li, Z. Ruan, Z. Tang, Z. Liu, Z. Wang, Y. Huang, Z. Pei, J.A. Zapien, C. Zhi, Initiating a mild aqueous electrolyte Co_3O_4/Zn battery with 2.2 V-high voltage and 5000-cycle lifespan by a Co(iii) rich-electrode, Energy Environ. Sci. 11 (2018) 2521–2530.

[30] C. Liu, X. Chi, Q. Han, Y. Liu, A High Energy Density Aqueous Battery Achieved by Dual Dissolution/Deposition Reactions Separated in Acid-Alkaline Electrolyte, Adv. Energy Mater. (2020) 1903589.

[31] G. Li, W. Chen, H. Zhang, Y. Gong, F. Shi, J. Wang, Membrane-Free Zn/MnO_2 Flow Battery for Large-Scale Energy Storage, Adv. Energy Mater. 1902085 (2020) 1–10.

[32] Z. Wang, J. Huang, Z. Guo, X. Dong, Y. Liu, Y. Wang, Y. Xia, A Metal-Organic Framework Host for Highly Reversible Dendrite-free Zinc Metal Anodes, Joule. 3 (2019) 1289–1300.

[33] H. Li, C. Xu, C. Han, Y. Chen, C. Wei, B. Li, F. Kang, Enhancement on Cycle Performance of Zn Anodes by Activated Carbon Modification for Neutral

Rechargeable Zinc Ion Batteries, J. Electrochem. Soc. 162 (2015) A1439–A1444.

[34] Q. Yang, Z. Lu, X. Sun, J. Liu, Ultrathin Co_3O_4 nanosheet arrays with high supercapacitive performance, Sci. Rep. 3 (2013) 1–7.

[35] Y. Li, X. Li, Z. Wang, H. Guo, T. Li, Distinct impact of cobalt salt type on the morphology, microstructure, and electrochemical properties of Co_3O_4 synthesized by ultrasonic spray pyrolysis, J. Alloys Compd. 696 (2017) 836–843.

[36] B. Chang, Z. Gu, Y. Guo, Z. Li, B. Yang, Glucose-assisted synthesis of Co_3O_4 nanostructure with controllable morphologies from nanosheets to nanowires, J. Alloys Compd. 676 (2016) 26–36.

[37] R. Torkzadeh-Mahani, M.M. Foroughi, S. Jahani, M. Kazemipour, H. Hassani Nadiki, The effect of ultrasonic irradiation on the morphology of NiO/Co_3O_4 nanocomposite and its application to the simultaneous electrochemical determination of droxidopa and carbidopa, Ultrason. Sonochem. 56 (2019) 183–192.

[38] Z. Xu, Y. Zeng, L. Wang, N. Li, C. Chen, C. Li, J. Li, H. Lv, L. Kuang, X. Tian, Nanoconfined phosphorus film coating on interconnected carbon nanotubes as ultrastable anodes for lithium ion batteries, J. Power Sources. 356 (2017) 18–26.

[39] S. Liang, X. Pei, W. Jiang, Z. Xu, W. Wang, K. Teng, C. Wang, H. Fu, X. Zhang, Free-standing dual-network red phosphorus@porous multichannel

carbon nanofibers/carbon nanotubes as a stable anode for lithium-ion batteries, Electrochim. Acta. 322 (2019) 134696.

[40] P. Hu, T. Zhu, X. Wang, X. Wei, M. Yan, J. Li, W. Luo, W. Yang, W. Zhang, L. Zhou, Z. Zhou, L. Mai, Highly Durable $Na_2V_6O_{16}\cdot 1.63H_2O$ Nanowire Cathode for Aqueous Zinc-Ion Battery, Nano Lett. 18 (2018) 1758–1763.

[41] Z. Yu, Z. Cheng, Z. Tai, X. Wang, C.M. Subramaniyam, C. Fang, S. Al-Rubaye, X. Wang, S. Dou, Tuning the morphology of Co_3O_4 on Ni foam for supercapacitor application, RSC Adv. 6 (2016) 45783–45790.

[42] H. Huang, S. Luo, C. Liu, Q. Wang, Y. Zhai, T. Yi, Synthesis of morphology controllable free-standing Co_3O_4 nanostructures and their catalytic activity for Li O_2 cells, Electrochim. Acta. 307 (2019) 232–240.

[43] W. Jiang, X. Xu, Y. Liu, L. Tan, F. Zhou, Z. Xu, R. Hu, Facile plasma treated β-MnO_2@C hybrids for durable cycling cathodes in aqueous Zn-ion batteries, J. Alloys Compd. 827 (2020) 154273.

[44] Q. Zhang, W. Xu, J. Sun, Z. Pan, J. Zhao, X. Wang, J. Zhang, P. Man, J. Guo, Z. Zhou, B. He, Z. Zhang, Q. Li, Y. Zhang, L. Xu, Y. Yao, Constructing Ultrahigh-Capacity Zinc-Nickel-Cobalt Oxide@$Ni(OH)_2$ Core-Shell Nanowire Arrays for High-Performance Coaxial Fiber-Shaped Asymmetric Supercapacitors, Nano Lett. 17 (2017) 7552–7560.

[45] W. Shang, W. Yu, P. Tan, B. Chen, H. Xu, M. Ni, A high-performance Zn battery based on self-assembled nanostructured $NiCo_2O_4$ electrode, J. Power Sources. 421 (2019) 6–13.

[46] D. Kong, J. Luo, Y. Wang, W. Ren, T. Yu, Y. Luo, Y. Yang, C. Cheng, Three-dimensional Co_3O_4@MnO_2 hierarchical nanoneedle arrays: Morphology control and electrochemical energy storage, Adv. Funct. Mater. 24 (2014) 3815–3826.

[47] F. Meng, H. Zhong, D. Bao, J. Yan, X. Zhang, In Situ Coupling of Strung Co_4N and Intertwined N-C Fibers toward Free-Standing Bifunctional Cathode for Robust, Efficient, and Flexible Zn-Air Batteries, J. Am. Chem. Soc. 138 (2016) 10226–10231.

[48] P. Tan, M. Liu, Z. Shao, M. Ni, Recent Advances in Perovskite Oxides as Electrode Materials for Nonaqueous Lithium-Oxygen Batteries, Adv. Energy Mater. 7 (2017) 1602674.

[49] F. Cheng, J. Chen, Lithium-air batteries: Something from nothing, Nat. Chem. 4 (2012) 962–963.

[50] P. Tan, Z. Wu, B. Chen, H. Xu, W. Cai, M. Ni, Exploring oxygen electrocatalytic activity and pseudocapacitive behavior of Co_3O_4 nanoplates in alkaline solutions, Electrochim. Acta. 310 (2019) 86–95.

[51] Q. Liu, C. Lu, Y. Li, Controllable synthesis of ultrathin nickel oxide sheets on carbon cloth for high-performance supercapacitors, RSC Adv. 7 (2017) 23143–23148.

[52] J. Jiang, J.P. Liu, X.T. Huang, Y.Y. Li, R.M. Ding, X.X. Ji, Y.Y. Hu, Q.B. Chi, Z.H. Zhu, General synthesis of large-scale arrays of one-dimensional nanostructured Co_3O_4 directly on heterogeneous substrates, Cryst. Growth Des.

10 (2010) 70–75.

[53] K. Wang, P. Pei, Z. Ma, H. Chen, H. Xu, D. Chen, X. Wang, Dendrite growth in the recharging process of zinc-air batteries, J. Mater. Chem. A. 3 (2015) 22648–22655.

[54] E.O. Aremu, D.J. Park, K.S. Ryu, The effects of anode additives towards suppressing dendrite growth and hydrogen gas evolution reaction in Zn-air secondary batteries, Ionics. 25 (2019) 4197-4207.

[55] W. Yu, W. Shang, P. Tan, B. Chen, Z. Wu, H. Xu, Z. Shao, M. Liu, M. Ni, Toward a new generation of low cost, efficient, and durable metal-air flow batteries, J. Mater. Chem. A. 7 (2019) 26744–26768.

[56] X. Wang, M. Li, Y. Wang, B. Chen, Y. Zhu, Y. Wu, A Zn-NiO rechargeable battery with long lifespan and high energy density, J. Mater. Chem. A. 3 (2015) 8280–8283.

[57] J. Liu, C. Guan, C. Zhou, Z. Fan, Q. Ke, G. Zhang, C. Liu, J. Wang, A Flexible Quasi-Solid-State Nickel–Zinc Battery with High Energy and Power Densities Based on 3D Electrode Design, Adv. Mater. 28 (2016) 8732–8739.

[58] P. Man, B. He, Q. Zhang, Z. Zhou, C. Li, Q. Li, L. Wei, Y. Yao, A one-dimensional channel self-standing MOF cathode for ultrahigh-energy-density flexible Ni– Zn batteries, J. Mater. Chem. A. 7 (2019) 27217–27224.

[59] P. Hu, T. Wang, J. Zhao, C. Zhang, J. Ma, H. Du, X. Wang, G. Cui, Ultrafast Alkaline Ni/Zn Battery Based on Ni-Foam-Supported Ni_3S_2 Nanosheets, ACS

Appl. Mater. Interfaces. 7 (2015) 26396–26399.

[60] J. Li, C. Chen, One-step facile synthesis of Ni_2P/C as cathode material for Ni/Zn aqueous secondary battery One-step facile synthesis of Ni_2P/C as cathode material for Ni/Zn aqueous secondary battery, Mater. Res. Express. 5 (2018) 015502.

[61] M. Gong, Y. Li, H. Zhang, B. Zhang, W. Zhou, J. Feng, H. Wang, Y. Liang, Z. Fan, J. Liu, H. Dai, Ultrafast high-capacity NiZn battery with NiAlCo-layered double hydroxide, Energy Environ. Sci. 7 (2014) 2025–2032.

[62] Y. Liu, J. Wang, S. Zeng, L. Zhou, W. Xu, D. Zheng, J. Liu, Y. Zeng, X. Lu, An ultrathin defect-rich Co_3O_4 nanosheet cathode for high-energy and durable aqueous zinc ion batteries, J. Mater. Chem. A. 7 (2019) 21678.

[63] W. Jiang, H. Wang, Z. Xu, N. Li, C. Chen, C. Li, J. Li, H. Lv, L. Kuang, X. Tian, A review on manifold synthetic and reprocessing methods of 3D porous graphene-based architecture for Li-ion anode, Chem. Eng. J. 335 (2018) 954–969.